Chapter 15
Structure, Morphology, and Spectroscopy Studies of $La_{1-x}RE_xVO_4$ Nanoparticles Synthesized by Various Methods

O. V. Chukova, S. Nedilko, S. G. Nedilko, A. A. Slepets, T. A. Voitenko, M. Androulidaki, A. Papadopoulos, and E. I. Stratakis

Abbreviations

IR	Infra Red
PL	Photo Luminescence
RE	Rare Earth
SEM	Scanning Electron Microscopy
UV	Ultra Violet
XRD	X-Rays Diffraction

15.1 Applications of Vanadate Matrices as Efficient Hosts for Luminescent RE^{3+} Ions

Vanadate matrices are well-known hosts for luminescent rare-earth (RE) ions since the middle of the twentieth century, when YVO_4:Eu^{3+} crystals became into mass usage as red phosphor for luminescent lamps, cathodoluminescent tubes, and oscillotrons [1–3]. The main reasons for the application of just vanadate matrix for mentioned purpose were high radiation and temperature hardness of oxides and high efficiency of RE^{3+} luminescence in vanadate matrix [3–6]. Excellent optical characteristics and other interesting structural, electrical, magnetic, and thermal

---

O. V. Chukova (✉) · S. Nedilko · S. G. Nedilko · A. A. Slepets · T. A. Voitenko
Taras Shevchenko National University of Kyiv, Kyiv, Ukraine
e-mail: chukova@univ.kiev.ua

M. Androulidaki · A. Papadopoulos · E. I. Stratakis
Institute of Electronic Structure & Laser (IESL) of Foundation for Research & Technology Hellas (FORTH), Heraklion, Greece

O. Fesenko, L. Yatsenko (eds.), *Nanocomposites, Nanostructures, and Their Applications*, Springer Proceedings in Physics 221,
https://doi.org/10.1007/978-3-030-17759-1_15

properties of vanadates have attracted wide research attention to development of this class of compounds for the last decades [7–11]. These compounds are chemically stable and nontoxic [12–14]. As a result, vanadate compounds have been considered for applications in many new areas and various technical and research fields involving chemistry and biology, optoelectronics, and renewable energy generation. Usually, each new practical application requires modifications of characteristics of materials due to special needs just of this application. Considering and comparing requirements from various areas of application, we can formulate the main direction for development of new vanadate compositions with improved usage characteristics.

Traditional application of vanadate materials as red phosphors for cathodoluminescent tubes is currently extended to wide area of applications of vanadate-based luminophors for various color imaging and lightening systems. The most promising direction is creation of new materials for converting violet and blue LED emission into white light [15–18]. Such application requires development of new compositions with enhanced efficiency of excitation from violet spectral range around 400 nm, whereas $REVO_4$ matrices usually have only edges of excitation located near 350 nm (Fig. 15.1) [19–21]. Replacement of the RE cations with alkaline earth (AE) cations (Ca^{2+}, Sr^{2+}, Ba^{2+}) in the RE vanadate nanoparticles was proposed recently to achieve arising of excitation effectiveness near 350–450 nm [22–25]. Similar behavior of excitation property was reported previously for several vanadate compounds. In fact, intensity and locations of excitation band of luminescence depend on material composition, concentration, and type of the AE cations. Maxima positions of this band were reported from 380 nm for $Zn_3V_2O_8$ [25], 385 for $Eu_{1-x}Ca_xVO_4$ [23], 389 nm for $Ca_2KZn_2(VO_4)_3$ [24], 393 for $Li_2Ca_2ScV_3O_{12}$:Eu^{3+} [22] to 405 nm for $La_{1-x-y}Eu_yCa_xVO_4$ [26] (Fig. 15.2).

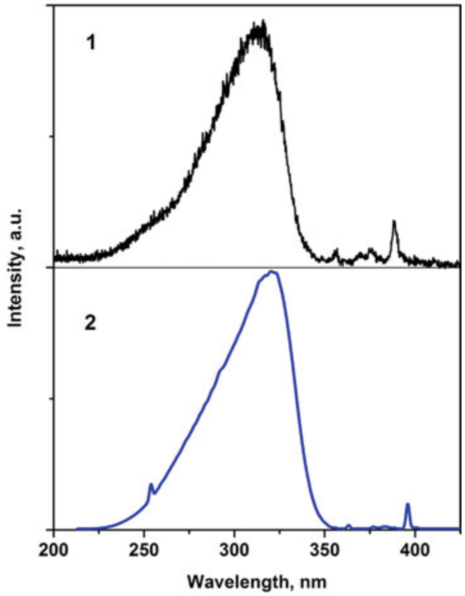

Fig. 15.1 Excitation spectra of the $La_{0.55}Eu_{0.45}VO_4$ (1) and $LaVO_4$:Eu,Li [21] (2) phosphors

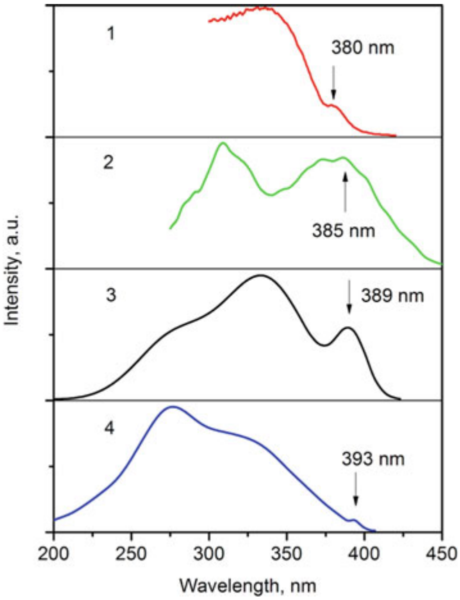

Fig. 15.2 Excitation spectra of the $Zn_3V_2O_8$ [25], $Eu_{1-x}Ca_xVO_4$ [23], $Ca_2KZn_2(VO_4)_3$ [22], and $Li_2Ca_2ScV_3O_{12}$:Eu^{3+} [24] phosphors

Nature of this excitation band is under discussion. It was ascribed to transitions in the vanadate groups [25], to presence of AE oxide impurity phases [22, 27], and to AE-induced defects [26]. It should be also noted that this excitation band is located in the range of f-f transitions in the Eu^{3+} ions, and sometimes it can be unrecognized in the spectra of the RE-doped vanadates [22]. Thus, additional complex investigation is needed to study AE effect on the RE ions luminescent properties in the vanadate matrices. So, development of new compositions with enhanced efficiency of excitation from violet range is an actual task in creation of vanadate compositions perspective for application in WLED devices.

The range of actual and potential biological applications of vanadates includes fluorescent probes for single molecule tracking, drug delivery and activation, protein detection, fluorescent bio labeling [14, 28, 29]. Some of these applications are used for investigation of living tissues and for therapy of diseases. In particular, singlet oxygen as an effective destroyer of cancer cells is used for the photodynamic therapy of tumors. The singlet oxygen could be produced at the decay of excited electronic states of some oxygen generating molecules, effective excitation of which is possible only from the near infra-red spectral region where absorption of living tissues is low. It is also carried out search of intermediating materials which are effectively excited by soft X-ray and can transfer excitation energy to oxygen generating molecules. Some oxide materials and orthovanadate compounds among them were considered as promising transferring media taking into account their stability in various neighboring and high absorption cross-section.

From the medical and biological points of view, materials for such applications should be safe to human body and have maximally possible high efficiency of energy transformation in order to decrease X-rays irradiation of patients. As the vanadate compounds are known as nontoxic materials, the main task for development of improved compositions for biological and medical applications is to increase luminescence emission efficiency without incorporation of some toxic agents.

Global demands in energy sector have also attracted attention to possible applications of luminescent nanoparticles in renewable energy sources, in particular, in solar energy. In this connection some vanadates have been proposed for creation of luminescent down-shifting coatings for silicon solar cells [30–33]. Currently, the most sold at the marked commercial silicon-based solar cells have efficiency of solar light to electrical energy conversion about 15%. The large part of the solar energy losses is associated with spectral mismatch of solar cells sensitivity and energy distribution in the solar spectrum. In order to cover this mismatch, "up" (from infrared (IR) to visible (VIS)) and "down" (from ultraviolet (UV) to VIS) conversions of solar photons are applied [34–37]. Considerable research efforts were devoted for the last years to development of materials for effective conversion of solar radiation, in particular dye-sensitization of solar cells that provides a low cost solution [38]. However, dye colors have tendency to degradation under UV irradiation; therefore, UV light is usually blocked by filters, and high-energy photons are not available for down-conversion. Possibility of luminescent absorbers application for adoption of UV light to working range of silicon solar cells was recently considered on the basis of thin inorganic crystalline films doped with RE ions [39, 40]. The RE-doped oxides are perspective candidates for this role due to their excellent thermal, mechanical, and optical properties. Various vanadate compositions such as multi-RE doped YVO_4 and Eu or Sm doped $LaVO_4$ vanadate nanoparticles were considered as promising materials for adaptation of incident solar light to spectral sensitivity of silicon solar cells. Arising of the above-described excitation band around 400 nm is a very desirable feature suitable for this application. Decreasing of cost is also especially important for materials proposed for covering of silicon solar cells.

For the last years, nanosized orthovanadates have been also considered as main perspective photocatalytic material in systems for visible light-driven photocatalytic water splitting. The widely used photocatalyst TiO_2 is active only under ultraviolet light irradiation [41, 42], while bismuth, cerium, and lanthanum orthovanadates are of a special attention as the most promising visible light-driven photocatalysts [43–45].

Summarizing, the wide range of vanadate compounds applications have attracted significant research efforts to development of new vanadate compositions with improved characteristics depending on requirements of various practical tasks. In particular, increase of excitation efficiency under light from near UV and violet spectral ranges is needed for solar energy conversion applications, whereas biological applications require light transformer materials safe to human body with high efficiency of energy transformation in order to decrease X-rays irradiation of living tissues. These goals can be achieved by isovalent and heterovalet doping of the basic $REVO_4$ compositions. In the present work we give overview of our 5-years research activities in these directions together with description and discussion of new results. The $LaVO_4$ matrix is used as basic for the study in order to achieve desirable cost decrease as the La reagents are among the cheapest RE reagents. Besides, the $LaVO_4$ matrix is characterized by one more unique for the orthovanadate compounds feature that is described in the next paragraph.

15.2 Feature of Lanthanum Vanadate Crystal Matrix Compared to Other Rare-Earth Vanadates

It is known that all the rare-earth orthovanadates ($REVO_4$) crystal compounds crystallize in the so-called zircon structure [46]. This rule has one exception and this exception is lanthanum vanadate ($LaVO_4$), which is dimorphic and can be stabilized in zircon or monazite crystal structures [47].

The zircon crystal structure is characterized by a tetragonal symmetry with space group I41/amd ($Z = 4$). In this structure, the La and V cations are located at high-symmetry positions; those can be described as formed by isolated VO_4 tetrahedral units surrounded by the La atoms forming eight-vertex LaO_8 polyhedrons. Each of V atoms is surrounded by four equivalent oxygen atoms forming the perfect VO_4 tetrahedrons with T_d local symmetry of oxygen surrounding and V–O distances near 1.7 Å (Fig. 15.3). In the LaO_8 dodecahedron, the La atoms are coordinated by eight oxygen atoms with identical four short bond lengths (2.2 Å) and four long bond lengths (2.5 Å) with D_{2d} local symmetry of oxygen surrounding [47–49]. Each VO_4 and LaO_8 polyhedron units are running parallel to the crystallographic c-axis. Each of the chains is joined laterally by edge-sharing LaO_8 dodecahedra.

The monazite structure (space group P21/n, No. 14, $Z = 4$) is another crystal structure adopted by $LaVO_4$ [50]. At ambient conditions this crystal structure is observed only for $LaVO_4$ among the $REVO_4$ family but can be obtained for several $REVO_4$ vanadates at high pressure [51]. In the monazite structure, the V and La atoms are four- and ninefold coordinated, respectively, with C_s local symmetry of oxygen surrounding for both the cations. The distorted VO_4 tetrahedrons only share corners and edges with the LaO_9 polyhedrons (Fig. 15.3).

Dimorphism of the $LaVO_4$ can be an essential advantage in the search of compositions with certain spectroscopy characteristics needed for one of the mentioned purposes, because luminescent properties of the RE^{3+} ions are known to be dependent on symmetry of crystal surrounding [49, 52–54]. It is also important to note here that isolated arrangement of the VO_4 tetrahedrons is a common feature for both the crystal structures which allows description of lattice vibrations as internal and external modes of this unit [55].

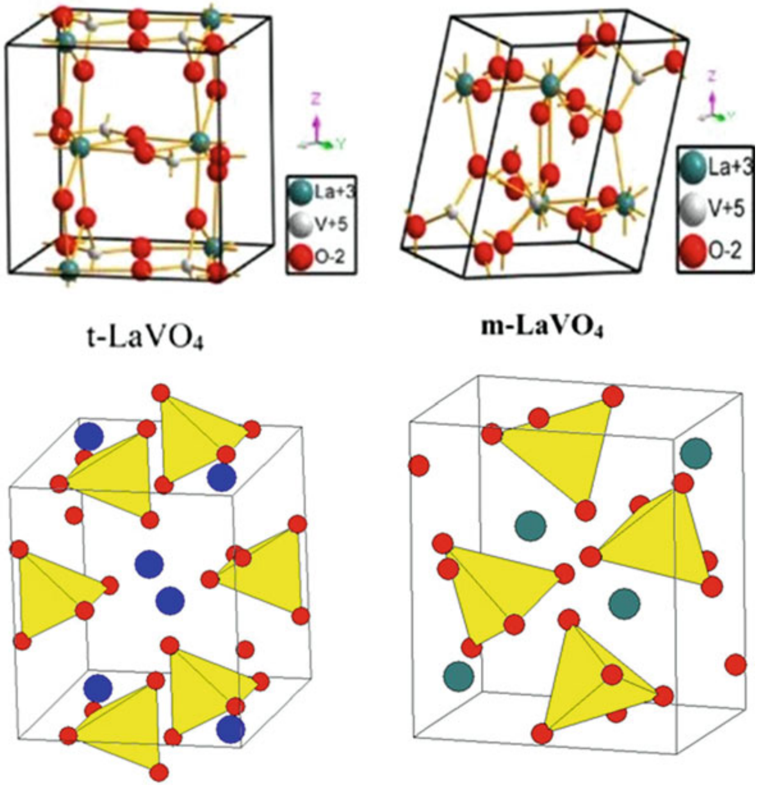

Fig. 15.3 Crystal structures of the $LaVO_4$ in zircon (left) and monoazite (right) phases shown in the form of atoms and bonds (top) and in the form of vanadate tetrahedrons and La atoms (bottom)

15.3 Methods of the Orthovanadate Nanoparticles Synthesis

As methods those could be successfully used for the synthesis of the orthovanadates nanoparticles, several authors have reported solid-state [20, 56], coprecipitation [21, 57], hydrothermal [58], solution combustion [59], and sol-gel synthesis [26, 60]. These methods could satisfy various reactivities of the compounds, homogenization, morphology, and sizes of nanoparticles; therefore, it was important for us to use various methods at the beginning of our work to find those ones that will allow us to achieve the best results in the noted above goals.

15.3.1 Solid-State Method

The La_2O_3 (99.99%), V_2O_5 (99.99%), and Eu_2O_3 (99.99%) powders were selected as the starting materials. For a typical process, all starting materials were weighed in the calculation stoichiometric ratio, and well mixed in the agate mortar. The mixed samples were calcinated using step-by-step heating (the step was 100 °C) up to 680 °C with 1 hour temperature exposure and intermediate grinding for each step. The final products were sintered for 6 hours at 900 °C (Fig. 15.4a).

15.3.2 Coprecipitation Method

The La_2O_3 and Eu_2O_3 starting materials were first dissolved into concentrated nitric acids. The stoichiometric ratios of the rare-earth nitrates solutions were mixed homogenously. After being stirred for half an hour the pH value was adjusted to about 7.0–8.0 with ammonia solution. Simultaneously, the Na_3VO_4 solutions were added into the solutions of $La(NO_3)_3$ and $Eu(NO_3)_3$. After this, the solutions were stirred until they became homogeneous. After being deposited for several days, they were filtered and dried in a drying box and the precursors were achieved. Then, they were thoroughly homogenized and calcinated in a muffle furnace using step-by-step heating up to temperature 680 °C with 1 hour temperature exposure and intermediate grinding for each 100 °C. Then the samples were heat-treated for 6 hours at 900 °C (Fig. 15.4b).

15.3.3 Sol-Gel Synthesis

Stoichiometrically calculated amounts of $La(NO_3)_3$, $Eu(NO_3)_3$, NH_4VO_3, and $Ca(NO_3)_2$ were used as a starting compound. The necessary quantities of the reagents were gradually mixed by 100, 20, 10, and 5 ml pipettes in a 250 ml beaker. The solution system was homogenized using a magnetic stirrer. The content of metal ions in their solutions was estimated out by the trilonometric method: solution of calcium nitrate was established by direct titration with murexide; the concentration of rare-earth ions in their respective nitrate solutions was established by direct titration with xylenol orange [61]. The NH_4VO_3 solution was titrated by using a hydroquinone with sulfuric acid before switching from blue to green and red. Ferroin was used as an indicator. At the next stage, a complexing agent was added to prevent the sedimentation process from the reaction mixture of a similar composition using the deposition method. Then 5 g of citric acid were dissolved in a 100 ml glass by distilled water, in which it was heated and added to the reagents solution. Such a mixture was poured into a graphite cup and placed on a sand bath. The solution gradually evaporated and turned into a gel, and then a powder. The

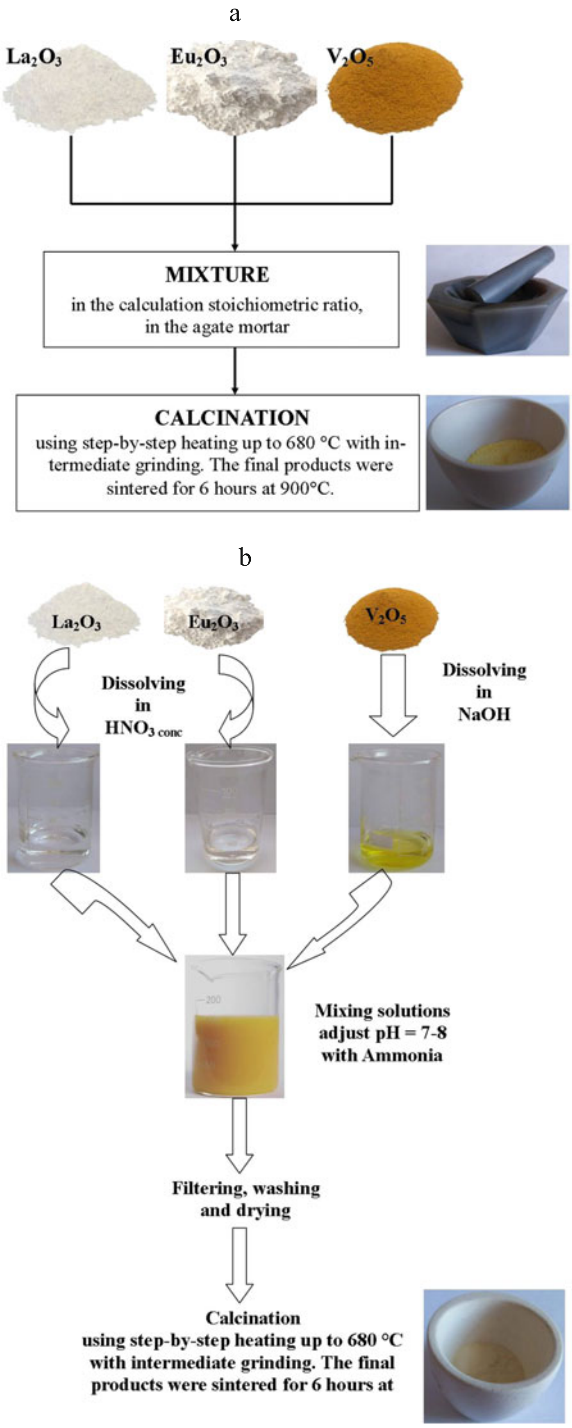

Fig. 15.4 Schematic diagram showing the experimental process for solid-state (**a**), coprecipitation (**b**), and sol-gel [26] (**c**) synthesis of the vanadate nanoparticles

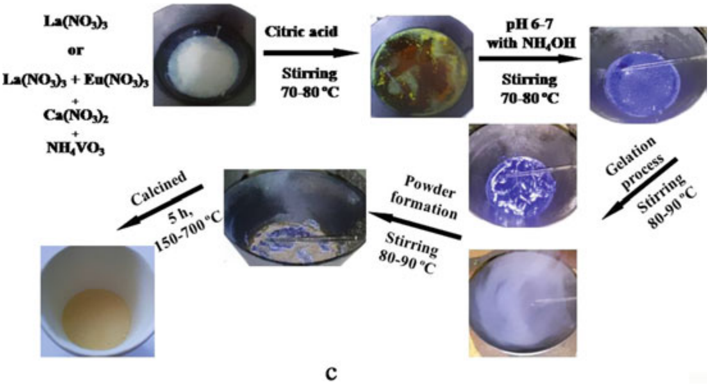

Fig. 15.4 (continued)

fine-grained powder was calcined for 5 hours at a step-by-step heating with 100 °C steps up to 680 °C temperature (Fig. 15.4c).

15.4 Phase Composition of the Synthesized Nanoparticles

Phase compositions and crystal lattice parameters of the synthesized samples were determined using X-ray diffractometer (XRD) DRON-3M ($Cu_{K\alpha}$-radiation with a Ni filter). The diffraction patterns were taken with a 2 deg/min step.

The XRD analysis has shown that all the synthesized samples $La_{1-x}Eu_xVO_4$ are single phase. XRD patterns of synthesized pure $LaVO_4$ are well matched with a standard card of monoclinic $LaVO_4$ (JCPDS PDF2 50-0367) for all the applied methods of synthesis (Fig. 15.5). Thus, crystal structure of pure $LaVO_4$ is monoclinic (space group $P2_1/n$, monazite structure family).

Crystal structure of the $La_{0.95}Eu_{0.05}VO_4$ samples synthesized by the coprecipitation method is also monoclinic. Further increase in the quantities of europium impurities ($x = 0.1$) leads to formation of two phase mixtures (the monoclinic and tetragonal). Finally, the crystal structure of $La_{0.7}Eu_{0.3}VO_4$ sample with a high substitution degree, $x = 0.3$, is tetragonal, belonging to the I41/amd space group. Thus, increasing Eu^{3+} ions concentration in $La_{1-x}Eu_xVO_4$ compositions synthesized by coprecipitation method leads to stabilization of the tetragonal phase. Crystal structures of the $La_{1-x}Eu_xVO_4$ samples with $x \geq 0.1$ are tetragonal (space group I41/amd zircon structure family) for solid-state and sol-gel methods of synthesis. Therefore, presence of europium ions with concentrations from $x \geq 0.1$ leads to change of the crystal structure from monoclinic to tetragonal [20, 21].

The XRD patterns of the $La_{1-x-y}Eu_yCa_xVO_4$ ($x \leq 0.2$, $y \leq 0.2$) samples are shown in Fig. 15.6. The $La_{0.9}Eu_{0.05}Ca_{0.05}VO_4$ sample with low concentration of the Ca^{2+} and Eu^{3+} impurities is also attributed to the monoclinic structure. Proximity

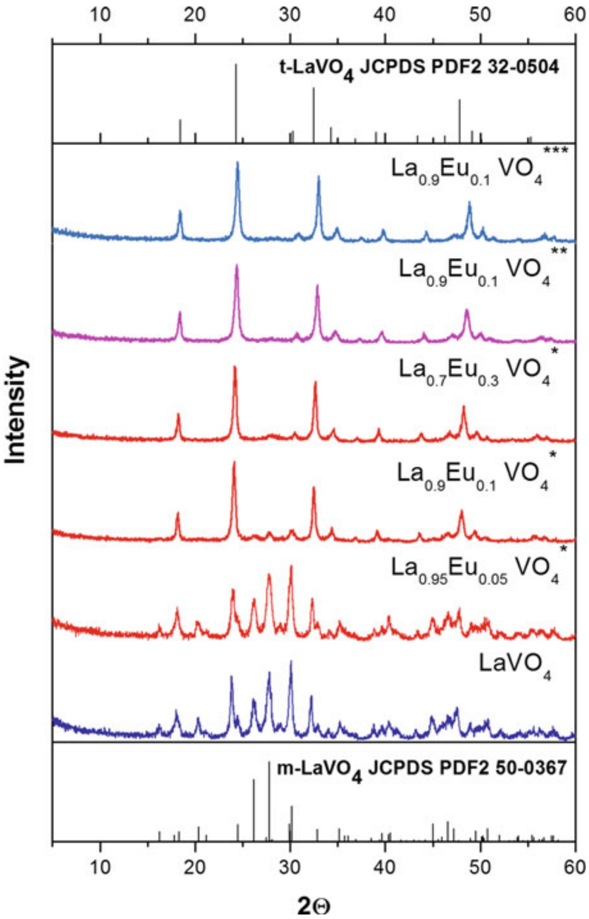

Fig. 15.5 XRD patterns of the La_{1-x} Eu_xVO_4 samples with $0 \leq x \leq 0.3$ synthesized by $_*$, coprecipitation method; $_{**}$, sol-gel method; $_{***}$, solid-state method

of the Ca^{2+} (1.12 nm), La^{3+} (1.16 nm), and Eu^{3+} (1.066 nm) ions radii provides an opportunity for calcium and europium ions incorporation into three plus cation's sites. Besides, we see that small quantities of the $Ca^{2+}(x \leq 0.1)$ and Eu^{3+} ions $(y \leq 0.05)$ can enter into the crystal lattice without change of the monoclinic $LaVO_4$ structure. Increasing concentrations of the $Eu^{3+}$and Ca^{2+}impurities lead to the formation of the monoclinic and tetragonal phase mixture. The $La_{0.6}Eu_{0.2}Ca_{0.2}VO_4$ sample becomes related to tetragonal structure, belonging to the I41/amd space group. This result is in agreement with the standard card of tetragonal $LaVO_4$ (JCPDS PDF2 32-0504) (see Fig. 15.5) [26]. Therefore, increasing the europium and calcium ions concentration in $La_{1-x-y}Eu_yCa_xVO_4$ $(x, y \leq 0.2)$ solid solutions leads to the change of the crystal structure with the formation of two phase compositions and subsequent stabilization of the tetragonal at $x = y = 0.2$.

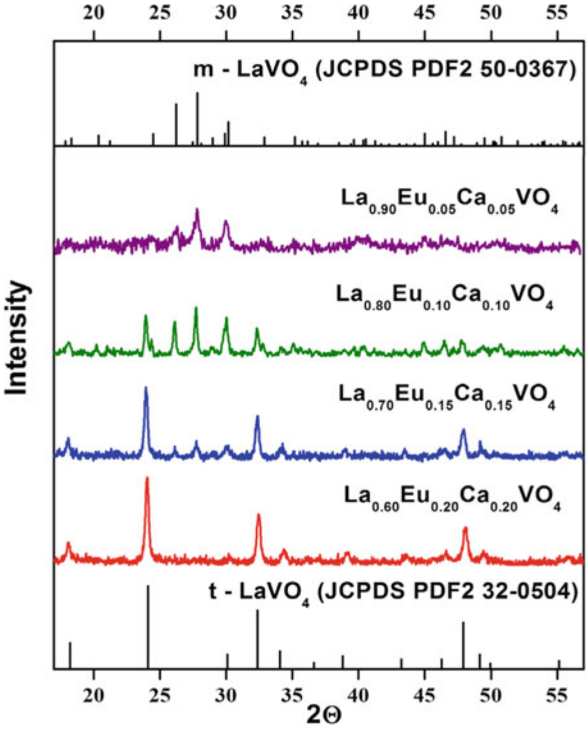

Fig. 15.6 XRD patterns of the $La_{1-x-y}Eu_yCa_xVO_4$ ($x = y = 0.2$) samples

15.5 Chemical Elements Analysis of the Ca-Doped Vanadate Nanoparticles

Chemical elements analysis was performed for the Ca-doped $La_{1-x-y}Eu_yCa_xVO_4$ samples in order to confirm arrangement of the Ca^{2+}cations in vanadate nanoparticles with $LaVO_4$ crystal structure, where cation sites usually have 3+ charge. We have investigated 3–5 various agglomerates or grains for each sample using the EDS tool of MIRA3 TESCAN Scanning Electron Microscope. Monitoring area from which information about content of atoms has been taken was larger than e-beam size, and it was near $(30 - 40) \times (30 - 40)$ μm. We have found that La, Eu, Ca, V, and O are the main components of the samples. The measured contents of the La^{3+} ions in the synthesized samples were quite close to the expected compositions [26]. Total contents of the Eu^{3+} and Ca^{2+} ions are also close to the expected compositions. However, the predicted simultaneous fourfold increase of ions Eu^{3+} and Ca^{2+} content (from 0.05 up to 0.20 at. %) is not implemented for the actual synthesized samples. We have observed that when the content of the Eu^{3+} ions increases by ~10 times, the content of the Ca^{2+} ions increases only by ~ 2–3 times. This is due both to specific of the samples (heterogeneity of sizes, shapes, and thickness of grains of powder, etc.) and features of the method (a significant error for light elements, the effect of electron beam on oxide surfaces, etc.). This result will be taken into account in the discussion of the synthesized compounds spectral properties.

15.6 Morphology of the Vanadate Nanoparticles Synthesized by Different Methods

Influence of method of synthesis on morphology of the $La_{1-x}Eu_xVO_4$ was studied on comparison of SEM images of nanoparticles synthesized by coprecipitation and sol-gel methods. The images were obtained from MIRA3 TESCAN microscope. SEM images of the samples in Figs. 15.7 and 15.8 show as large areas up to ~ 2 × 2 μm for general view of samples as well as small separated areas up to ~ 0.8 × 0.8 μ.

Coprecipitated samples consist of nanoparticles that are agglomerated in grains of different sizes from tens of nanometers to 1 micron. There are many pores and cavities between nanoparticles in grains. Each of the samples consists of nanoparticles of similar shapes and sizes; the latter are increased with increasing of Eu concentration from 20–40 nm for $x = 0.1$ to 50–70 nm for $x = 0.3$ (Fig. 15.7). The shapes of nanoparticles have slightly distinguished round-polyhedral forms.

Sol-gel samples consist of nanoparticles that are densely agglomerated in solid grains with sizes about 0.5–2.0 microns (Fig. 15.8). Sizes of nanoparticles vary from 40 to 60 nm for samples of all the concentrations. Dependence of morphology on Eu concentration for the sol-gel nanoparticles was not observed. The shapes of nanoparticles cannot be analyzed correctly due to high rate of agglomerization. Thus, we should make a conclusion that coprecipitation allows us to obtain nanoparticles with lower rates of agglomeration and smaller sizes of nanoparticles for the samples with low Eu concentration. Note that the described differences in morphology of the nanoparticles can affect their spectral properties.

The SEM images of the $La_{1-x-y}Eu_yCa_xVO_4$ samples are shown in Fig. 15.9 [26]. The samples are formed by nanoparticles of size from 20 to 100 nm. The $La_{0.9}$ $Eu_{0.05}Ca_{0.05}VO_4$ samples with low concentration of the Eu and Ca impurities consist of grains of 0.1–0.2 μ size; those are formed by nanoparticles of 10–20 nm size (Fig. 15.9c). The nanoparticles of larger size, ~ 100 nm, are characteristic for the samples with higher concentration of dopants, $La_{0.8}Eu_{0.1}Ca_{0.1}VO_4$. Most of them have polyhedral shapes with clearly defined edges and angles between them (Fig. 15.9d). The particles with the observed polyhedral shapes have to be assigned to the crystal system of lower symmetry. Thus, the observed polyhedral shapes can be regarded as a manifestation of the monoclinic phase in the studied samples. The next increase of the Eu^{3+} and Ca^{2+} dopants concentrations also generates particles of ~100 nm sizes (Fig. 15.9e). Despite the poor quality of this image, it is possible to conclude that the shapes of the particles are closer to the cylinders and rods. The same shapes are observed for the samples of the highest dopants concentration, $La_{0.6}Eu_{0.2}Ca_{0.2}VO_4$ (Fig. 15.9f). However, it should be noted that size of the particles is smaller for these samples; it is preferably 30–60 nm.

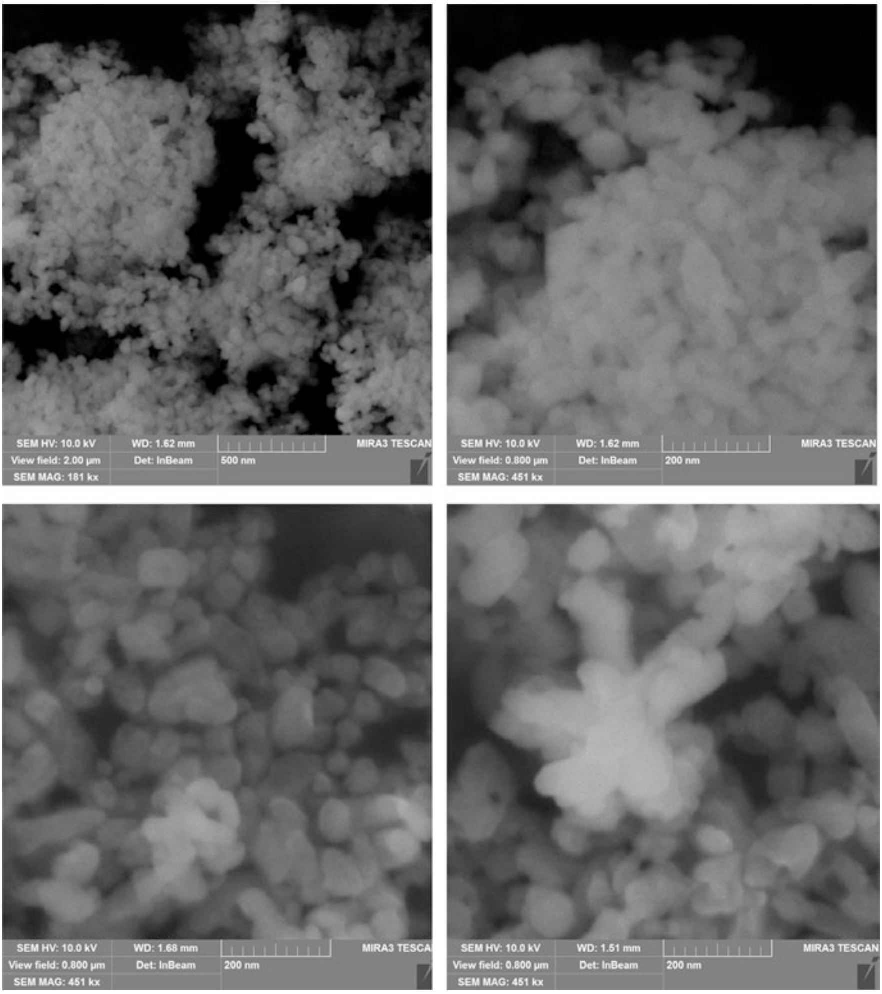

Fig. 15.7 The SEM images of the $La_{1-x}Eu_xVO_4$ nanoparticles synthesized by coprecipitation method $x = 0.1$ (**a**, **b**), 0.2 (**c**), 0.3 (**d**)

Thus, we can say that the change of the powder samples composition is accompanied by the changes in the size and morphology of their constituent particles. These changes are consistent with the XRD data on the structure and phase composition of the samples. Therefore, the SEM data can be interpreted as indicating that the samples of higher dopants concentration are mixtures of monoclinic and tetragonal phases and the content of the latter increases when the content of europium and calcium ions increases.

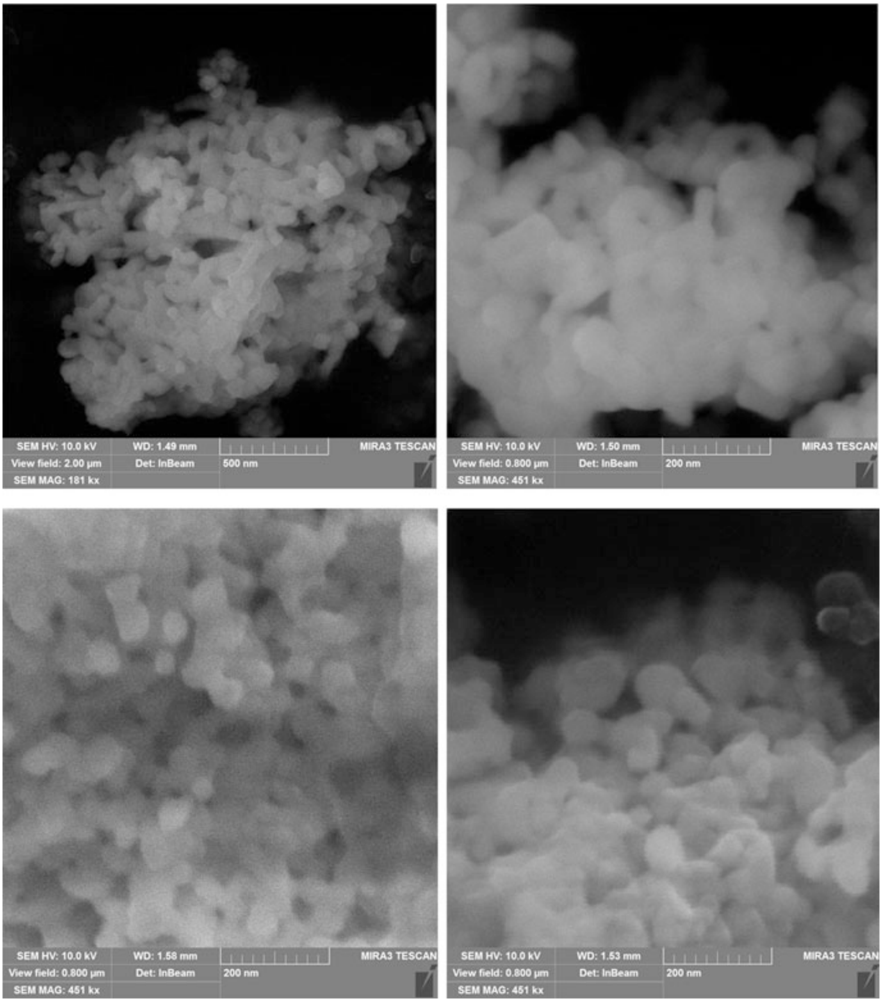

Fig. 15.8 The SEM images of the $La_{1-x}Eu_xVO_4$ nanoparticles synthesized by the sol-gel method $x = 0.1$ (**a**, **b**), 0.2 (**c**), 0.3 (**d**)

15.7 Infrared Spectroscopy

Infrared spectra (IR) of the samples were recorded in the 400–400 cm^{-1} range on Perkin Elmer IR spectrometer using the KBr pellet method.

The view of the IR spectra in the range of 400–1100 cm^{-1} (Fig. 15.10) is typical for the $LaVO_4$ IR- absorption spectra measured previously in this range [62–64].

It is well known that the bending (ν_2 and ν_4) and stretching vibrations (ν_1 and ν_3) of O–V–O bonds of the $VO_4{}^{3-}$ anion form IR absorption spectra of various orthovanadates in the range 400–700 and 700–1100 cm^{-1}, respectively [65, 66].

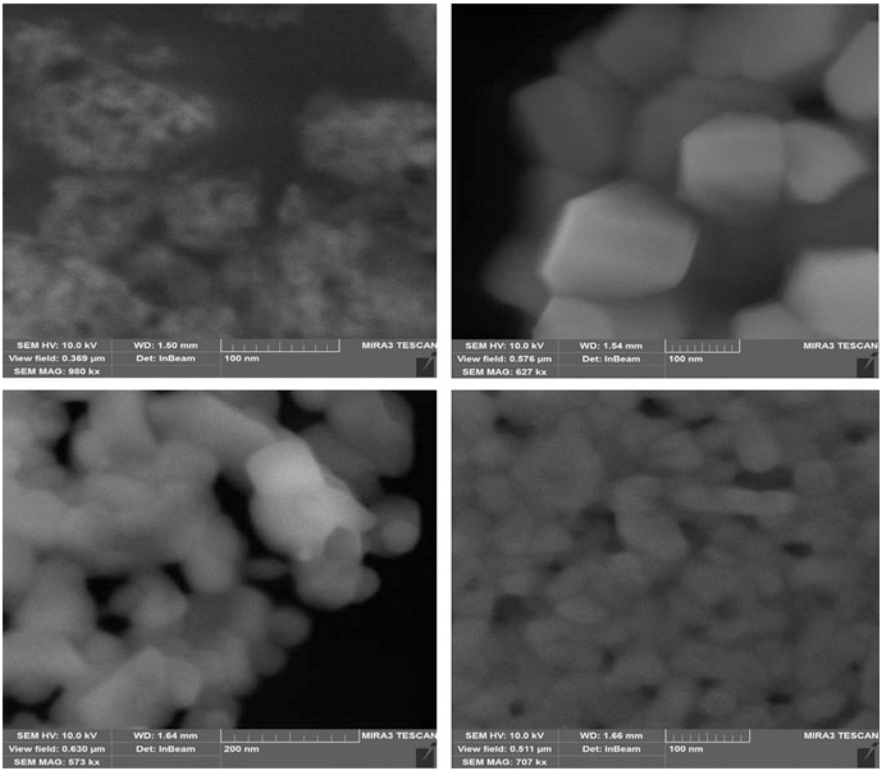

Fig. 15.9 The SEM images of the $La_{1-x-y}Eu_yCa_xVO_4$ synthesized by sol-gel method $x = y = 0.05, 0.1, 0.15, 0.2$

In fact, measured by us spectrum of the un-doped $LaVO_4$ contains separated weak band located in the range 400–700 cm^{-1}, while the main wide band is located in the range 700–1100 cm^{-1} (Figs. 15.10 and 15.11). Sharp peak at 434 cm^{-1} and blurred band centered near 550 cm^{-1} compose IR spectra of this sample in the former range. The main peak at ~ 778 cm^{-1} and three strongly overlapped other ones located at ~ 820, 850, and 880 cm^{-1} form wide band (Fig. 15.11, curve 1). (All the mentioned peaks are marked by arrows close to curve 1 in Fig. 15.11, and their positions are in Table 15.1).

In the spectra of the $La_{1-x}Eu_xVO_4$ samples synthesized by various methods, there are two main strong peaks at 859 and 892 cm^{-1}. This fact is consistent with the results published for the tetragonal $LaVO_4$ [65, 67]. We find that t-$LaVO_4$ has similar vibrational peaks positions with m-$LaVO_4$ (see the table), but as it can be seen from Fig. 15.10, deformation vibrational peaks ν_4 for t-$LaVO_4$ have lower intensity than for the m-$LaVO_4$. Also, increased number of vibrational peaks in the range 750–900 cm^{-1} is observed for m-$LaVO_4$ for all the applied methods of synthesis (see arrows in Figs. 15.10 and 15.11). Thus, six or seven peaks can be

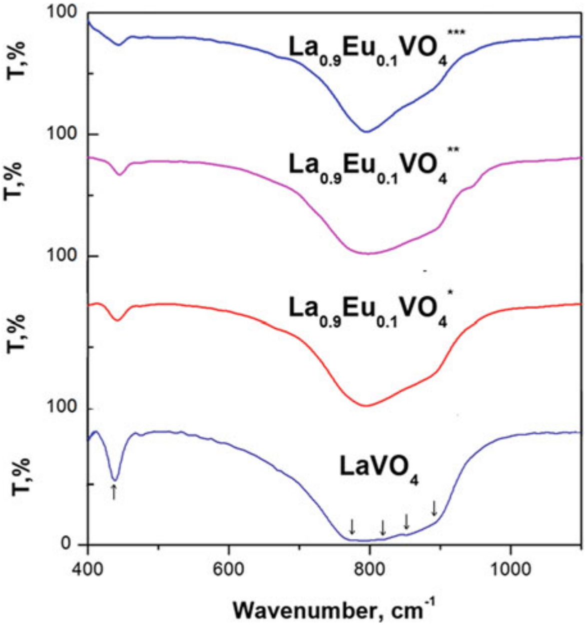

Fig. 15.10 IR absorption spectra of the $La_{0.9}Eu_{0.1}VO_4$ nanoparticles synthesized by $_*$, coprecipitation method; $_{**}$, sol-gel method; $_{***}$, solid-state method; and $LaVO_4$ nanoparticles synthesized by solid-state method

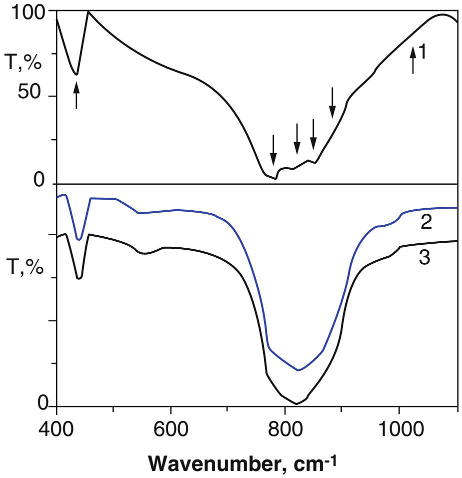

Fig. 15.11 IR absorption spectra of the $LaVO_4$ (1), $La_{0.8}Eu_{0.1}Ca_{0.1}VO_4$ (2), and $La_{0.6}Eu_{0.2}Ca_{0.2}VO_4$ (3) nanoparticles synthesized by sol-gel method

distinguished there, and shape and structure of the band become very similar to the ones previously published on the IR absorption spectra of the $LaVO_4$ [65, 67]. The exact assignment of spectral components to a certain type of modes is difficult, especially that concerning stretching vibration range. Due to the low C_s symmetry of the VO_4^{3-} molecular anion in monoclinic $LaVO_4$, four IR lines lying close to each other can appear in this range of spectra. Our experimental findings are in good agreement with the theoretical prediction noted above. Mentioned fact causes

Table 15.1 IR peaks positions (in cm^{-1}) and their attributions to vibration modes in the VO_4^{3-} vanadate groups

$LaVO_4$	$La_{0.9}Eu_{0.1}VO_4$ Solid state	$La_{0.9}Eu_{0.1}VO_4$ Coprecipitation	$La_{0.9}Eu_{0.1}VO_4$ Sol-gel	$La_{0.8}Eu_{0.1}Ca_{0.1}VO_4$	Vibration modes
434	440	439	440	439	ν_4
				553	
778				783	
820	800	803	801	802, 821	
850	821	820	821	835; 854	ν_3
	858	859	859		
880	889	890	890	875	ν_1
1026	920	922	924	918; 978	

strong overlapping of the lines, that is why they are revealed as one complex wide band.

Doping with calcium ions causes a distortion of certain amount of vanadate groups. As a result, additional peaks near 553 cm^{-1} appear in the spectrum. Besides, as we have shown above all co-doped samples are a mixture of monoclinic and tetragonal $LaVO_4$ phases and contribution of the phases depends on the dopants concentration. The VO_4^{3-} molecular groups possess D_{2d} symmetry in tetragonal $LaVO_4$. So, two lines of E_u and A_{2u} symmetry can be found in the range of stretching vibrations if morphology of the VO_4^{3-} groups corresponds to an ideal tetragonal lattice structure. Really, neighbor environment and symmetry of some VO_4^{3-} groups in tetragonal lattice are also deformed by Ca^{2+} ions and all of VO_4^{3-} internal vibrations can occur in the IR spectra. As previously have been reported the calculated [68] and measured [67] peaks positions of the IR- absorption lines for tetragonal $LaVO_4$ are close to those for monoclinic $LaVO_4$. Thus, the eight lines can form the range of stretching vibrations, we suppose. Change of the phase composition leads to mentioned changes of the shape of the IR bands and their positions. Regarding published theoretical and experimental data a possible assignment of all measured features was made (Table 15.1). Additional studies are necessary in order to clarify the origin of the bands that are in the ranges 500–700 and 900–1000 cm $^{-1}$. We can only note that similar features were previously observed in the IR absorption spectra of some Ca containing orthovanadates [69, 70].

In any cases, we are able to state that observed IR spectra confirm that anionic sublattice of studied vanadates is built by VO_4^{3-} molecular anions.

15.8 Reflectance Spectroscopy

Reflectance spectroscopy of the samples was performed using Perkin Elmer Lambda 950 spectrometer. The powder samples were pressed in a sample holder and then spectra of diffuse reflection were measured. In the used mode, the monochromator is placed before the samples and all light reflected from the powder samples are collected by photometric sphere. In experimental solution luminescence of the investigated samples could give additional contribution in the recorded spectra and this possibility should be taken into account under analysis of the obtained spectra.

Reflection bands of the undoped $LaVO_4$ nanoparticles are observed in the 250–500 nm spectral range (Fig. 15.12). Maxima of the reflection bands are placed near 300 and 315 nm for the nanoparticles obtained by coprecipitation and sol-gel methods, respectively. The 50% reflection is observed near 340 and 350 nm, respectively. Adding of the Eu^{+} activator ions causes weak narrow peaks at 536, 465, and 395 nm. Also strong decrease of the 300 nm band with increase of the Eu^{3+} concentration is observed. It is accompanied by appearance of the additional peak at 280 nm and increase of the reflection around 250 nm for the samples obtained by all applied methods of synthesis. This effect was also observed for the sol-gel samples co-doped with Ca^{2+} ions. Spectra of the Ca^{2+}-co-doped samples contain also two additional wide reflection bands around 400 and 500 nm. The bands are strong and can achieve at the spectral maxima up to 70–80% reflection compared with the main 300 nm band.

The main band at 300 nm can be attributed to the inner O^{2-} ➔ V^{5+} charge transfer transitions in the $VO_4{}^{3-}$ vanadate groups [71–74]. The narrow peaks at 536, 465, and 395 nm are caused by $^7F_0 \rightarrow {}^5D_{2,3,4}$ *f-f* transitions in the Eu^{3+} ions. The wide bands around 400 and 500 nm that were observed for the Ca^{2+}-co-doped samples should be connected with transitions in Ca-induced defect centers. Their structure will be discussed below together with discussions of luminescence properties. Decrease of the 300 nm band with increase of the Eu^{3+} concentration is obviously connected with contribution of the luminescence emission in the recorded spectra, and it should be discussed together with the analysis of the excitation spectra.

15.9 Luminescent Spectroscopy

15.9.1 Dependencies of Luminescence Properties of the $La_{1-x}Eu_xVO_4$ Nanoparticles on Methods of Synthesis

Luminescence spectra were investigated using ACTONi (500) monochromator with grating 150 grooves/mm (blaze @ 300 nm), slit on 50 micron and liquid N_2 – cooled CCD registration as well as DFS12 monochromator with grating 600 grooves/mm, and slit on 50 micron and FEU-79 photomultiplier registration. Luminescence spectra were excited with 325, 405, 478, and 532 nm diode lasers or powerful Xenon lamp [see for additional details 75, 76].

Fig. 15.12 Reflection spectra of the investigated vanadate nanoparticles

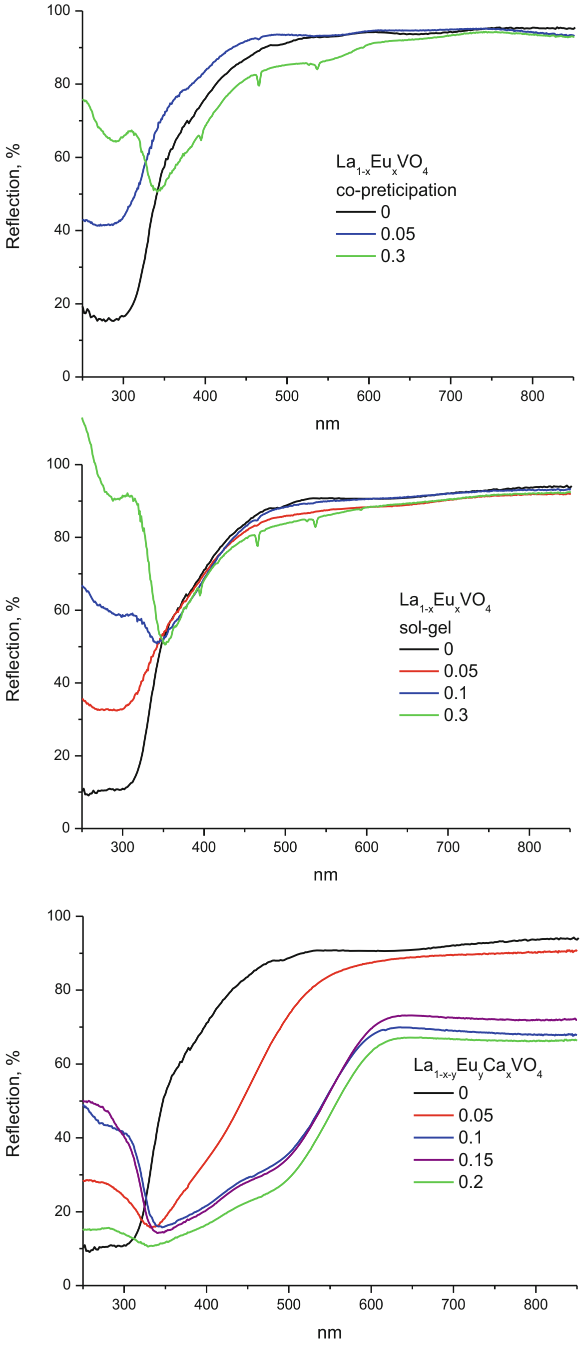

Emission of the $La_{1-x-y}Eu_yVO_4$ samples was observed in the 550–730 nm spectral range and they consist of narrow spectral lines (Fig. 15.13). Undoubtedly, those lines are caused by radiation transitions in Eu^{3+} ions. Peculiarities of fine structure of the spectra and their intensities depend on method of synthesis and on the Eu^{3+} concentration. This is clearly demonstrated in Fig. 15.13 using laser excitation with 325 nm. The similar effect was also observed before at synchrotron excitations with shorter wavelengths [20]. At 300 nm excitation, the peaks located at 587, 621, 687, and 698 nm are the best seen for the samples with the lowest Eu concentrations. Then they disappear at $x = 0.1$ for the samples obtained by the solid-state method, whereas these lines are clearly revealed at concentration $x = 0.1$ for the samples obtained by the coprecipitation method (Fig. 15.3b, curve 2). For the samples with $x = 0.3$, the noted lines disappear for the samples obtained by both methods of synthesis. It was also shown previously that structure of emission spectra of the $La_{1-x-y}Eu_yVO_4$ nanoparticles does not essentially depend on excitation wavelength [20].

The observed dependencies can be assigned to transformation from monoclinic phase to tetragonal phase (see XRD analysis Chapter above). Really, the observed luminescence lines in the 580–720 nm spectral range are by the $^5D_0 \rightarrow {}^7F_J$ ($J = 0, 1, 2, 3, 4$) electron radiation transitions in the inner $4f^n$ shell of the Eu^{3+} ions. The

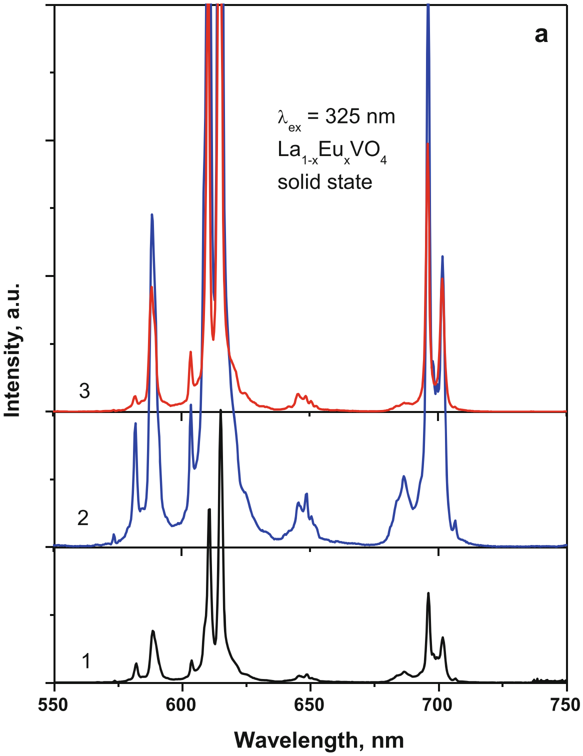

Fig. 15.13 (**a**) Emission spectra of the $La_{1-x}Eu_xVO_4$ nanoparticles synthesized by solid-state method, $\lambda_{ex} = 325$ nm, $x = 0.05$ (1), 0.1 (2) and 0.3 (3). (**b**) Emission spectra of the $La_{1-x}Eu_xVO_4$ nanoparticles synthesized by coprecipitation method, $\lambda_{ex} = 325$ nm, $x = 0.05$ (1), 0.1 (2) and 0.3 (3). (**c**) Emission spectra of the $La_{1-x}Eu_xVO_4$ nanoparticles synthesized by sol-gel method, $\lambda_{ex} = 325$ nm, $x = 0.05$ (1), 0.1 (2) and 0.3 (3)

Fig. 15.13 (continued)

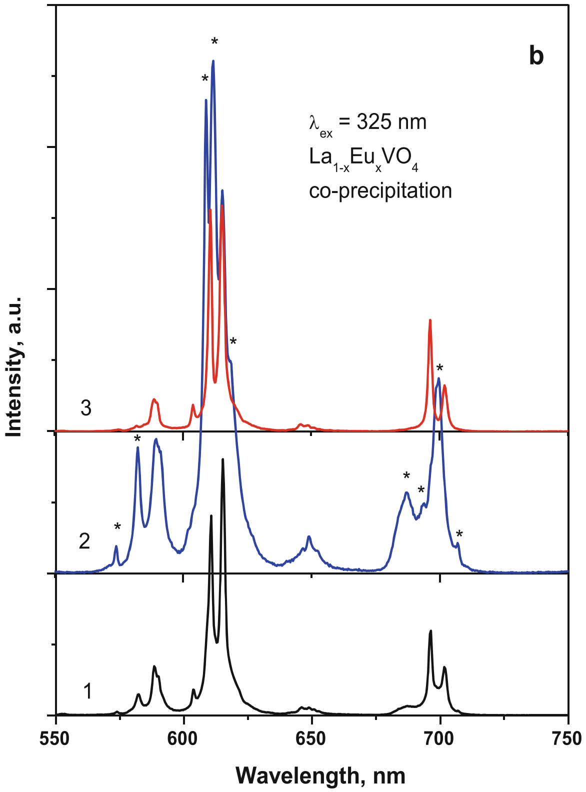

^7F_J energy levels may be split in the crystal field on the $2j + 1$ sub-levels, but some of possible transitions can be forbidden by the symmetry rules [77]. If the Eu^{3+} ions occupy the site of the La^{3+} ions in tetragonal $LaVO_4$ crystal lattice (I41/amd space group), they have D_{2d} site symmetry. In such a case, group theory predicts no luminescence peaks from $^5D_0 \rightarrow {}^7F_0$ transition, two lines from the $^5D_0 \rightarrow {}^7F_1$ and three lines from the $^5D_0 \rightarrow {}^7F_2$ transitions. If the Eu^{3+} ions occupy the site of the La^{3+} ions in monoclinic $LaVO_4$ crystal lattice ($P2_1/n$ space group), they have C_1 site symmetry. In this case, group theory predicts manifestation of all possible transitions: one luminescence peak from the $^5D_0 \rightarrow {}^7F_0$ transition, three lines from $^5D_0 \rightarrow {}^7F_1$, and five lines from the $^5D_0 \rightarrow {}^7F_2$ transitions [48, 49].

It is clearly seen from Fig. 15.13 that noted expectations are exactly realized for the investigated nanoparticles. So, for the samples with low europium content, we have observed three lines in the $J = 1$ range and five lines in the $J = 2$ range (marked by the arrows in Fig. 15.3, curves 1). (Lines in the $J = 3$ range have weak intensity, lines in the $J = 4$ range are strongly overlapped, that is why it is difficult to separate for these ranges all spectral components of emission transitions.) Thus, properties of luminescence spectra for vanadates of the noted composition obtained by both methods reveal monoclinic structure of their lattice. Therefore, for

Fig. 15.13 (continued)

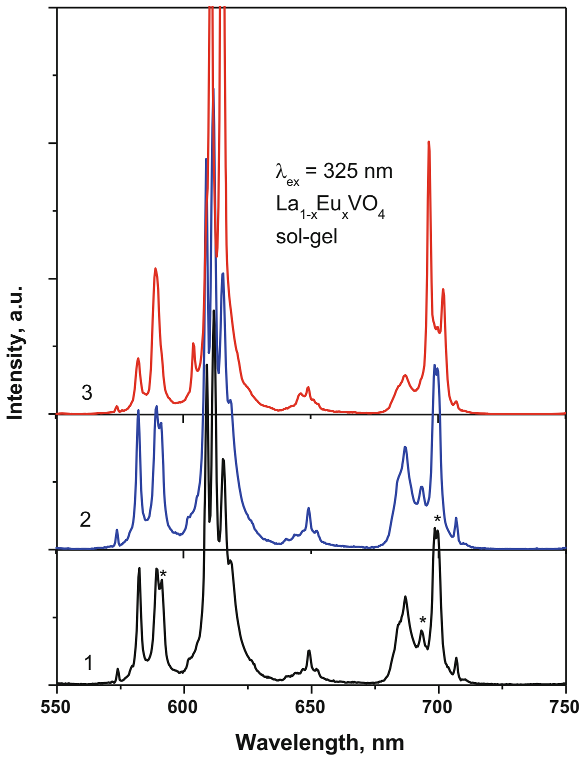

these compositions the Eu^{3+} ions are impurities substituting the La^{3+} ions without changes of crystal lattice. With increasing of the europium content, transformation of crystal lattice structure from monoclinic to tetragonal occurs. This is reflected in transformation of spectra; structure of those at $0.1 \leq x \leq 0.3$ corresponds to high symmetry coordination of the Eu^{3+} ions by oxygen ions.

It has to be emphasized that transformation of the spectra with increasing of the Eu^{3+} concentration takes place with different rates for compounds synthesized by the different methods. For the samples obtained by solid-state method, we have observed at $x = 0.1$ the spectra that completely corresponded to the Eu^{3+} arrangement in tetragonal vanadate structure (Fig. 15.13a), whereas for the same vanadate obtained by coprecipitation and sol-gel methods spectral lines characteristic for monoclinic vanadates remain also at $x = 0.1$ (Fig. 15.13b and c). These effects should be more prominent for the Ca-doped samples, where co-existence of monoclinic and tetragonal phases is observed up to $x = 0.15$ (Fig. 15.5).

15.9.2 *Influence of Ca-Doping on Luminescence Properties of the Sol-Gel $La_{1-x}Eu_xVO_4$ Nanoparticles*

Structure and intensity of the $La_{1-x-y}Eu_yCa_xVO_4$ samples emission depend on impurity concentration (Fig. 15.14) and excitation wavelength (Fig. 15.15 [26]).

For the $La_{0.8}Eu_{0.1}Ca_{0.1}VO_4$ sample, which is just a mixture of monoclinic and tetragonal phases (see Fig. 15.5), the photoluminescence (PL) lines at 586, 592.5, 607, 611, 614, 618, 649, 697, and 702 nm (marked by the arrows in Fig. 15.15, curve 2) are observed at all the applied λ_{ex}. (We call this set of the lines as "first set.") Note also that the ratio of intensity of the lines at 611, 614, and 618 nm changes if λ_{ex} varies. Besides, intensive lines at 580, 590, 591.7, 595.6, 608.7, and 622 and lines near 645, 651, 655, 706, and 708 nm (marked by arrows with asterisk at Fig. 15.15, curve 3) are distinctively observed in the spectra measured at $\lambda_{ex} = 405$ nm. (We call this set of the lines as "second set.") So, the measured emission spectra are the superposition of two sets of luminescence lines. Since we have shown above that the sample $La_{0.8}Eu_{0.1}Ca_{0.1}VO_4$ is just a mixture of two crystalline phases, we have first to suppose that these sets are related to emission

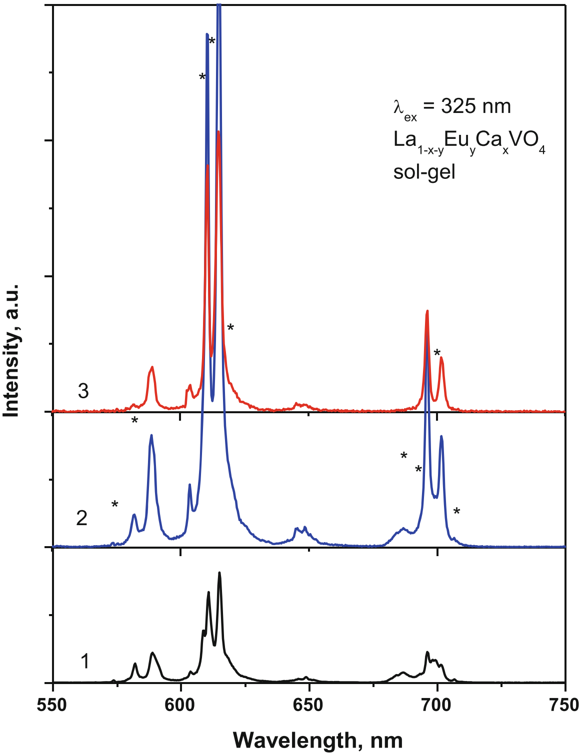

Fig. 15.14 (**a**) Emission spectra of the $La_{1-x-y}Eu_yCa_xVO_4$ nanoparticles synthesized by sol-gel method, $\lambda_{ex} = 325$ nm, $x = y = 0.1$ (1), 0.15 (2) and 0.2 (3). (**b**) Emission spectra of the $La_{1-x-y}Eu_yCa_xVO_4$ nanoparticles synthesized by sol-gel method, $\lambda_{ex} = 405$ nm, $x = y = 0.1$ (1), 0.15 (2) and 0.2 (3)

Fig. 15.14 (continued)

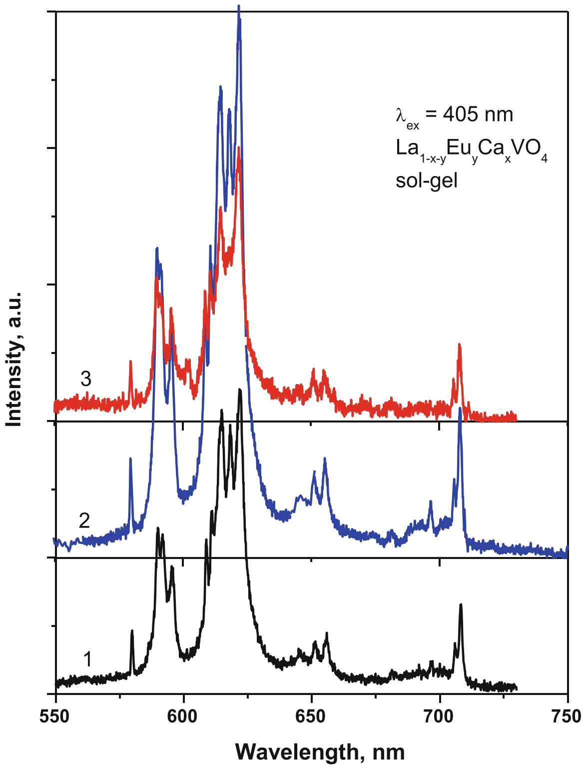

of Eu^{3+} centers in monoclinic and tetragonal phases as it was described above for the Ca-free $La_{1-x}Eu_xVO_4$ nanoparticles.

With the intent to clarify this assumption we performed study of the luminescence spectra dependence on the samples composition at the same excitation wave length, $\lambda_{ex} = 405$ nm (Fig. 15.14b). We found that the emission spectra of the samples where $x = 0.1$ and 0.15 are very close to each other. This finding agrees with the statement that these samples are the mixture of two phases. Tetragonal phase dominates in the $La_{0.6}Eu_{0.2}Ca_{0.2}VO_4$ sample, and we see that "second set" of the luminescence lines also dominates in the spectrum of this sample, but we see also that mentioned before line at 618 nm is vanished in this spectrum. Thus, we concluded that not only competition between content of the crystal phases influences luminescence behavior. Let's discuss this question in more detail.

So, it was not surprising that accounting the spectra in Fig. 15.15 in sum we have found one line for the $^5D_0 \rightarrow {}^7F_0$ (spectral range 570–585 nm), five lines (586, 592.5, 590, 591.7, 595.6 nm) for the $^5D_0 \rightarrow {}^7F_1$ (spectral range 585–600 nm), and seven lines (607, 614, 618, 608.7, 611, 614, 622 nm) for $^5D_0 \rightarrow {}^7F_2$ transitions (spectral range 600–650 nm), as this figure shows the luminescence spectra of the sample which is mixture of the monoclinic and tetragonal phases. This statement also concerns the spectra 1 and 2 in Fig. 15.14b, as they also represent luminescence

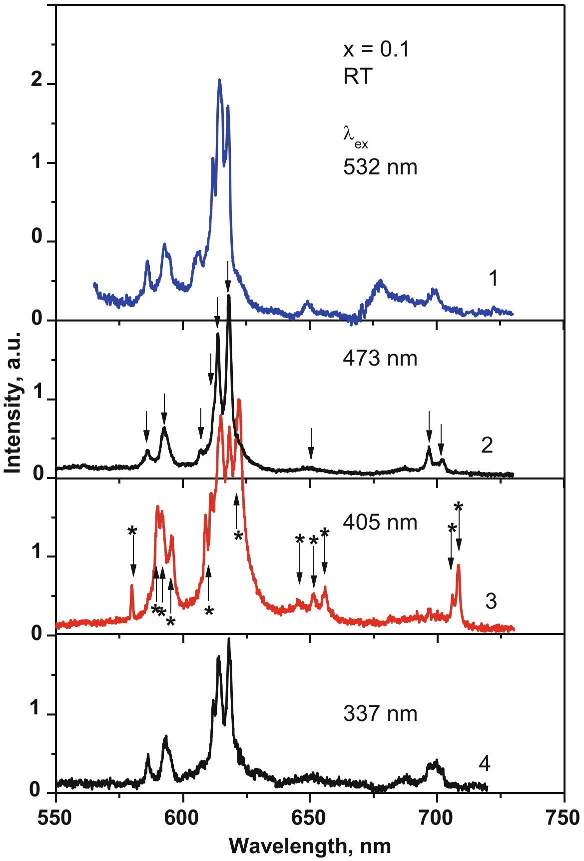

Fig. 15.15 Emission spectra of the $La_{0.8}Eu_{0.1}Ca_{0.1}VO_4$ nanoparticles at $\lambda_{ex} = 532$ (1, 5), 473 (2), 405 (3), and 337 nm (4) [26]

of the mixture, $x = 0.1$ and 0.15, respectively. It was surprising that we see intensive line from the $^5D_0 \rightarrow {}^7F_0$ transition for the $La_{0.6}Eu_{0.2}Ca_{0.2}VO_4$ sample which represents only a tetragonal crystal structure (Fig. 15.14b, curve 3). Thus, we supposed that spectral transformations shown in Figs. 15.14 and 15.15 are related also to role of Ca^{2+} cations, as their concentration increases by 2–3 times when going from $x = 0.1$ to 0.2 (see Sect. 3.2).

In fact, obtained results mean that at least two different types of luminescence centers formed by the ions Eu^{3+} in the sample of tetragonal structure contribute to the PL spectra. We ascribed the above-mentioned spectral lines to emission of type I ("first set" of lines) and type II of the centers ("second set" of lines). Emission line from the $^5D_0 \rightarrow {}^7F_0$ transition (580 nm) was observed only for the type II centers, and the most intensive lines of the $^5D_0 \rightarrow {}^7F_2$ and $^5D_0 \rightarrow {}^7F_4$ transitions for these centers are located at 622 and 708 nm, respectively. For type I centers, the most intensive lines are located at 614 and 697 nm. These spectral features allow us to do assumption that types I and II of centers are characterized by different symmetry of the Eu^{3+} ions environment: the type I centers are characterized by higher site symmetry and the type II centers are characterized by lower site symmetry in the crystal lattices [77]. We supposed that type I centers are formed by the Eu^{3+} ions in their regular positions in the crystal lattice (D_{2d} symmetry).

As for the type II centers, we suppose that they can be formed by Eu^{3+} ions disturbed by defects generated as a result of Ca^{2+} cations incorporation into $LaVO_4$ crystal lattice. Taking into account that above-noted lines of type II centers (e.g., lines at 622 and 708 nm) were not observed for the Ca^{2+}-free sample (Fig. 15.13), we concluded that the most possible origin of the type II centers is the Eu^{3+} ions disturbed by Ca-induced defects. In the case of the doped with calcium $LaVO_4$ lattice, the Ca^{2+} dopant has to replace the La^{3+} ions. Then, effective "-1" charge arises. Charge compensation of mentioned "-1" charge is needed, as the crystal has to be electroneutral. This compensation can be achieved via the formation of one oxygen vacancy, $[V_O]^{2+}$, on each two Ca^{2+}/La^{3+} replacements. Thus, for the Ca^{2+} dopants arrangement in the $LaVO_4$ crystal lattice, we should expect that some of the Eu^{3+} ions are under effect of both neighbor Ca^{2+} cations and oxygen vacancy. Thus, we can assume that such Eu^{3+} ions are just the type II of the luminescence centers, and their local symmetry is lower if comparing to symmetry of the type I centers. Taking into account that $^5D_0 \rightarrow {}^7F_0$ transition emission line (near 580 nm) is observed in the spectra (Figs. 15.14 and 15.15), the symmetry of type II centers may be C_2 or C_s [47–49]. The C_2 symmetry of the Eu^{3+} surrounding in the I41/amd space group of orthovanadates can be achieved only by equal distortions of two oxygen positions. Therefore, we assume that case of the C_s symmetry of the Eu^{3+} surrounding at the type II centers is more probable.

The observed differences in excitation spectra measured in the emission lines corresponded to different types of centers (614 and 622 nm for type I and II centers, respectively) confirm the made above assumptions [26]. The wide band at 320 nm was more intensive in the excitation spectra of type I centers. The 320 nm band was also observed in the spectra of the $La_{0.9}Eu_{0.1}VO_4$ sample (Fig. 15.16, curve 2). This band is caused by electron transitions in the vanadate VO_4^{3-} groups. Therefore,

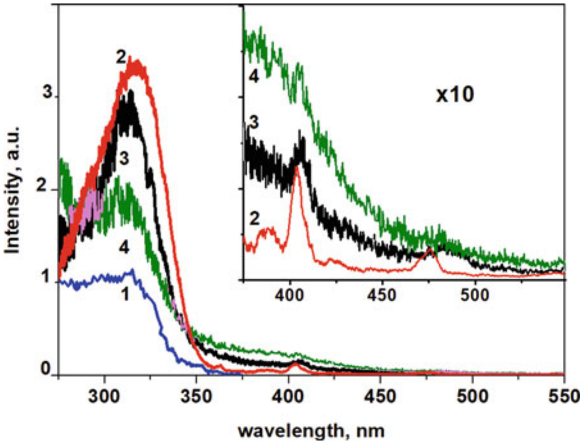

Fig. 15.16 Excitation spectra of the $LaVO_4$ (1), $La_{0.9}Eu_{0.1}VO_4$ (2), and $La_{0.6}Eu_{0.2}Ca_{0.2}VO_4$ (3, 4) sol-gel nanoparticles at $\lambda_{em} = 550$ (1), 614 (2, 3), and 622 nm (4); $T = 77$ K (1), T = RT (2–4)

the type I centers are better excited through the matrix than type II centers, which confirms our assumptions about relation of the type I centers with the Eu^{3+} ions in the regular positions in the crystal lattice.

15.10 Conclusions

The $La_{1-x}Eu_xVO_4$ ($0 \leq x \leq 0.4$) nanoparticles were synthesized by solid-state, coprecipitation, and sol-gel methods. The $La_{1-x-y}Eu_yCa_xVO_4$ ($0 \leq x, y \leq 0.2$) nanoparticles were synthesized by sol-gel method. Phase composition of the sample depends on the x, y values.

Increasing concentration of europium, Eu^{3+}, and calcium ions, Ca^{2+}, in $La_{1-x-y}Eu_yCa_xVO_4$ solid solutions causes changing of the crystal structure from monoclinic to tetragonal.

Phase transformation and especially Ca^{2+} ions influence IR spectroscopy and luminescence behavior of studied compounds, as Ca^{2+} ions impact both $VO_4{}^{3-}$ molecular groups conformation and La^{3+} and Eu^{3+} ions nearest neighborhood.

Emission of the investigated samples is observed in the 550–730 nm spectral range and it consists of narrow spectral lines. These lines are caused by the $^5D_0 \rightarrow {}^7F_J$ electron transitions in the Eu^{3+} ions.

The Eu^{3+} ions form two types of emission centers in the samples under study. The assumption was made that type I centers are formed by the Eu^{3+} ions in their regular positions in the crystal lattice, while the type II centers have complex structure, and they consist of Eu^{3+} ions, Ca^{2+} cations, and oxygen vacancies.

Acknowledgments This project has received funding from Ministry of Education and Science of Ukraine and from the EU-H2020 research and innovation program under grant agreement No 654360 having benefited from the access provided by Institute of Electronic Structure & Laser (IESL) of Foundation for Research & Technology Hellas (FORTH) in Heraklion, Crete, Greece within the framework of the NFFA-Europe Transnational Access Activity.

References

1. Palilla FC, Levine AK, Rinkevics M (1965) Rare earth activated phosphors based on yttrium orthovanadate and related compounds. J Electrochem Soc 112(8):776
2. Blasse G, Bril A (1969) Luminescence of phosphors based on host lattices ABO4 (A is Sc, In; B is P, V, Nb). J Chem Phys 50:2974
3. Palilla FC, Levine AK (1966) YVO4:Eu: a highly efficient, red-emitting phosphor for high pressure mercury lamps. Appl Opt 5:1467–1468
4. Panayiotakis G, Cavouras D, Kandarakis I, Nomicos C (1996) A study of X-ray luminescence and spectral compatibility of europium-activated yttrium-vanadate (YVO4: Eu) screens for medical imaging applications. Appl Phys A Mater Sci Process 62(5):483–486
5. Krumpel AH, van der Kolk E, Cavalli E, Boutinaud P, Bettinelli M, Dorenbos P (2009) Lanthanide 4f-level location in $AVO_4:Ln^{3+}$ (A = La, Gd, Lu) crystals. J Phys Condens Matter 21:115503–115508

6. Panchal V, Errandonea D, Segura A, Rodríguez-Hernandez P, Muñoz A, Lopez-Moreno S, Bettinelli M (2011) The electronic structure of zircon-type orthovanadates: effects of high-pressure and cation substitution. J Appl Phys 110:043723
7. Kang JH, Im WB, Lee DC, Kim JY, Jeon DY, Kang YC, Jung KY (2005) Correlation of photoluminescence of (Y,Ln)VO_4:Eu^{3+} (Ln = Gd and La) phosphors with their crystal structures. Solid State Commun 133:651–656
8. Wang Q, Zhang Z, Zheng Y, Cai W, Yifei Y (2012) Multiple irradiation triggered the formation of luminescent $LaVO_4$: Ln^{3+} nanorods and in cellulose gels. CrystEngComm 14:4786
9. Xu Z, Li C, Hou Z, Peng C, Lin J (2011) Morphological control and luminescence properties of lanthanide orthovanadate LnVO4 (Ln = La to Lu) nano−/microcrystals via hydrothermal process. CrystEngComm 13:474–482
10. Li K, Van Deun R (2018) Eu^{3+} /Sm^{3+} −doped $Na_2BiMg_2(VO_4)_3$ from substitution of Ca^{2+} by Na^+ and Bi^{3+} in $Ca_2NaMg_2(VO_4)_3$: color-tunable luminescence via efficient energy transfer from $(VO_4)^{3-}$ to Eu^{3+} /Sm^{3+} ions. Dyes Pigments 155:258–264
11. Venkatesan R, Velumani S, Ordon K, Makowska-Janusik M, Corbel G (2018) Nanostructured bismuth vanadate ($BiVO_4$) thin films for efficient visible light photocatalysis. Mater Chem Phys 205:325–333
12. Mialon G, Gohin M, Gacoin T, Boilot J-P (2008) High temperature strategy for oxide nanoparticle synthesis. ACS Nano 2(12):2505–2512
13. Venkataraman BV, Sudha S (2005) Vanadium toxicity. Asian J Exp Sci 19(2):127–134
14. Clark AS, Fagant JM, Mitch WE (1985) Selectivity of the insulin-like actions of vanadate on glucose and protein metabolism in skeletal muscle. Biochem J 232:273–276
15. Biswas P, Kumar V, Padha N, Swart HC (2017) Synthesis, structural and luminescence studies of $LiSrVO_4$:Sm^{3+} nanophosphor to fill amber gap in LEDs under n-UV excitation. J Mater Sci Mater Electron 28:6159–6168
16. Nakajima T, Isobe M, Tsuchiya T, Ueda Y, Kumagai T (2008) Direct fabrication of metavanadate phosphor films on organic substrates for white-light-emitting devices. Nat Mater 7:735–740
17. Shinde KN, Singh R, Dhoble SJ (2014) Photoluminescent characteristics of the single-host white-light-emitting $Sr_{3-3x/2}(VO_4)_2$:xEu (0<x<0.3) phosphors for LEDs. J Lumin 146:91–96
18. Lin H-Y, Chang W-F, Chu S-Y (2013) Luminescence of $(Ca,Sr)_3(VO_4)_2$:Pr^{3+},Eu^{3+}phosphor for use in CuPc-based solar cells and white light-emitting diodes. J Lumin 133:194–199
19. Lisiecki R, Ryba-Romanowski W, Cavalli E, Bettinelli M (2010) Optical spectroscopy of Er^{3+}-doped $LaVO_4$ crystal. J Lumin 130:131–136
20. Chukova O, Nedilko S, Nedilko SG, Sherbatsky V, Voitenko T (2013) Comparable structural and luminescent characterization of the $La_{1-x}Eu_xVO_4$ solid solutions synthesized by solid state and co-precipitation methods. Solid State Phenom 200:186–192
21. Park SW, Yang HK, Chung JW, Moon BK, Choi BC, Jeong JH (2010) Enhanced red emission of $LaVO_4$:Eu^{3+} phosphors by Li-doping. J Korean Phys Soc 57:1764–1768
22. Xue C, Xia Z (2013) Luminescence properties of $Li_2Ca_2ScV_3O_{12}$ and $Li_2Ca_2ScV_3O_{12}$:Eu^{3+} synthesized by solid-state reaction method. Opt Mater 35:2736–2739
23. Chukova OV, Nedilko SG, Slepets AA, Nedilko S, Voitenko TA (2018) Synthesis and investigation of La,Ca -doped $EuVO_4$ nanoparticles with enhanced excitation by near violet light. Phys Status Solidi A 215:1700894–1700897
24. Krishna Bharat L, Jeon S-K, Gopi Krishna K, Yu JS (2017) Rare-earth free self-luminescent $Ca_2KZn_2(VO_4)_3$ phosphors for intense white light-emitting diodes. Sci Rep 7:42348
25. Li T, Luo J, Honda Z, Fukuda T, Kamata N (2012) Sintering condition and optical properties of $Zn_3V_2O_8$. Phosphor Adv Mater Phys Chem 2:173–177
26. Chukova OV, Nedilko SG, Slepets AA, Nedilko SA, Voitenko TA (2017) Synthesis and properties of the $La_{1-x-y}Eu_yCa_xVO_4$, ($0 \leq x, y \leq 0.2$) compounds. Nanoscale Res Lett 12:340–311
27. Bhatkar VB (2013) Synthesis and luminescence properties of yttrium vanadate based phosphors. Int J Eng Sci Innov Technol 2:426–432

28. Yang P, Huang S, Kong D, Lin J, Fu H (2007) Luminescence functionalization of SBA-15 by YVO4:Eu 3+ as a novel drug delivery system. Inorg Chem 46(8):3203–3211
29. Shen J, Sun L-D, Yan C-H (2008) Luminescent rare earth nanomaterials for bioprobe applications. Dalton Trans 42(14):5661–5808
30. Chornii V, Chukova O, Nedilko SG, Nedilko S, Voitenko T (2016) Enhancement of emission intensity of $LaVO_4:RE^{3+}$ luminescent solar light absorbers. Phys Status Solidi C 13(1):40–46
31. Nedilko SG, Chornii V, Chukova O, Degoda V, Bychkov K, Terebilenko K, Slobodyanik M (2016) Luminescence properties of the new complex La,$BiVO_4$: Mo,Eu compounds as materials for down-shifting of VUV–UV radiation. Radiat Meas 90:282–286
32. Van der Ende BM, Aarts L, Meijerink A (2009) Lanthanide ions as spectral converters for solar cells. Phys Chem Chem Phys 11:11081–11095
33. Kumar V, Khan AF, Chawla S (2013) Intense red-emitting multi-rare-earth doped nanoparticles of YVO 4 for spectrum conversion towards improved energy harvesting by solar cells. J Phys D Appl Phys 46:365101–365109
34. Lewis NS, Nocera DG (2006) Powering the planet: chemical challenges in solar energy utilization. Proc Natl Acad Sci U S A 103:15729–15735
35. Morton O (2006) Solar energy: a new day dawning? Silicon Valley sunrise. Nature 443:19–22
36. Van der Zwaan B, Rabl A (2003) Prospects for PV: a learning curve analysis. Sol Energy 74:19–31
37. Goetzberger A, Hebling C, Schock HW (2003) Photovoltaic materials. History, status and outlook. Mater Sci Eng R 40:1–46
38. Huang X, Han S, Huang W, Liu X (2013) Enhancing solar cell efficiency: the search for luminescent materials as spectral converters. Chem Soc Rev 42:173–201
39. Henderson B, Imbusch GF (1989) Optical spectroscopy of inorganic solids. Oxford University Press, Oxford, 657 p
40. Auzel F (2005) Up-conversions in RE-doped solids. In: Liu G, Jacquier B (eds) Spectroscopic properties of rare earths in optical materials. Springer, Berlin, pp 266–319
41. Li W, Li D, Lin Y, Wang P, Chen W, Fu X, Shao Y (2012) Evidence for the active species involved in the photodegradation process of methyl orange on TiO_2. J Phys Chem 116(5):3552–3560
42. Wang D, Li R, Zhu J, Shi J, Han J, Zong X, Li C (2012) Photocatalytic water oxidation on $BiVO_4$ with the electrocatalyst as an oxidation cocatalyst: essential relations between electrocatalyst and photocatalyst. J Phys Chem 116(8):5082–5089
43. Zhang Y, Li G, Yang X, Yang H, Lu Z, Chen R (2013) Monoclinic $BiVO_4$ micro-/nanostructures: microwave and ultrasonic wave combined synthesis and their visible-light photocatalytic activities. J Alloys Compd 551:544–550
44. Sivakumar V, Suresh R, Giribabu K, Narayanan V (2015) $BiVO_4$ nanoparticles: preparation, characterization and photocatalytic activity. Cogent Chem 1:1074647
45. Yang X, Zuo W, Li F, Li T (2015) Surfactant-free and controlled synthesis of hexagonal $CeVO_4$ nanoplates: photocatalytic activity and superhydrophobic property. ChemistryOpen 4:288–294
46. Hazen RM, Finger LW (1979) Crystal structure and compressibility of zircon at high pressure. Am Mineral 64:196–201
47. Errandonea D, Garg AB (2018) Recent progress on the characterization of the high-pressure behaviour of AVO4 orthovanadates. Prog Mater Sci 97:123–169
48. Chukova OV, Nedilko SG, Slepets AA, Nedilko S, Voitenko TA (2017) Crystal field effect on luminescent characteristics of europium doped orthovanadate nanoparticles, proceedings of the 2017 IEEE 7th international conference on nanomaterials: applications and properties. NAP 2017:81903497–81903495
49. Park SW, Yang HK, Chung JW, Chen Y, Moon BK, Cho BC, Jeon JH, Kim JH (2010) Photoluminescent properties of $LaVO_4$ Eu^{3+} by structural transformation. Physica B 405:4040–4044
50. Errandonea D, Pellicer-Porres J, Martinez-Garcia D, Ruiz-Fuertes J, Friedrich A, Morgenroth W, Popescu C, Rodríguez-Hernández P, Muñoz A, Bettinelli M (2016) Phase Stability of Lanthanum Orthovanadate at High Pressure. J Phys Chem C 120:13749–13762

51. Errandonea D, Achary SN, Pellicer-Porres J, Tyagi AK (2013) Pressure-induced transformations in PrVO4 and SmVO4 and isolation of high-pressure metastable phases. Inorg Chem 52:5464–5469
52. Chukova O, Nedilko S, Scherbatskyi V (2012) Effect of annealing on luminescence properties of the undoped and rare earth doped lead tungstate crystals. Opt Mater 34:2071–2075
53. Zorenko Y, Gorbenko V, Voloshinovskii A, Stryganyuk G, Nedilko S, Degoda V, Chukova O (2005) Luminescence of Sc-related centers in single crystalline films of Lu $_3Al_5O_{12}$ garnet. Phys Status Solidi C 2:105–108
54. Malashkevich GE, Chukova OV, Nedilko SG, Shevchenko GP, Bokshyts YV, Kouhar VV (2016) Influence of gold nanoparticles on luminescence of Eu^{3+} ions sensitized by structural defects in germanate films. J Phys Chem C 120:15369–15377
55. Santos CC, Silva EN, Ayala AP, Guedes I, Pizani PS, Loong CK, Boatner LA (2007) Raman investigations of rare earth orthovanadates. J Appl Phys 101:053511
56. Huang Y, Seo H (2013) Structure and luminescence of new red-emitting materials-Eu^{3+-}doped triple orthovanadates $NaALa(VO_4)_2$ (A = Ca, Sr, Ba). J Am Ceram Soc 96:1181–1187
57. Chukova O, Nedilko S, Nedilko SG, Voitenko T, Gomenyuk O, Sheludko V (2015) Study of temperature behavior of luminescence emission of $LaVO_4$ and $La_{1-x}Eu_xVO_4$ powders. Solid State Phenom 230:153–159
58. Xu Z, Li C, Hou Z, Peng C, Lin J (2011) Morphological control and luminescence properties of lanthanide orthovanadate LnVO4 (Ln = La to Lu) nano-/microcrystals via hydrothermal process. CrystEngComm 13:474–482
59. Yoon SJ, Park K (2014) Synthesis and photoluminescent properties of white-emitting $Sr_{2.91}V_2O_8$:0.06:Eu^{3+} phosphors. Opt Mater 36:1305–1310
60. Chumha N, Kittiwachana S, Thongtem T, Thongtem S, Kaowphong S (2014) Synthesis and characterization of $GdVO_4$ nanostructures by a tartaric acid-assisted sol–gel method. Ceram Int 40:16337–16342
61. Chukova OV, Nedilko SG, Slepets AA, Nedilko S, Voitenko TA, Virko SV Influence of Ca^{2+} impurities on structure, morphological and optical characteristics of Eu_xVO_4 and $La_{1-x}Eu_xVO_4$ luminescent nanoparticles, Proceedings of the 2018 IEEE 8th international conference on nanomaterials: applications and properties, NAP 2018, volume, accepted paper
62. Liu J, Li Y (2007) Synthesis and self-assembly of luminescent Ln^{3+}-doped $LaVO_4$ uniform Nanocrystals. Adv Mater 19:1118–1122
63. Liu G, Duan X, Li H, Dong H (2009) Hydrothermal synthesis, characterization and optical properties of novel fishbone-like $LaVO_4$:Eu^{3+} nanocrystals. Mater Chem Phys 115:165–171
64. Escobar Von ME, Baran EJ (1978) Uber die tetragonale Modifikation von Lanthan-orthowanadat. Z Anorg Allg Chem 441:273–277
65. Nakamoto K (1963) Infrared spectra of inorganic and coordination compounds. Wiley, New York, p 410
66. Lax M (1974) Symmetry principles in solid state and molecular physics, vol 499. Wiley, New York
67. Fang ZM, Hong Q, Zhou ZH, Dai SJ, Weng WZ, Wan HL (1999) Oxidative dehydrogenation of propane over a series of low-temperature rare earth orthovanadate catalysts prepared by the nitrate method. Catal Lett 61:39–44
68. Sun L, Zhao X, Li Y, Li P, Sun H, Cheng X, Fan W (2010) First-principles studies of electronic, optical and vibrational properties of $LaVO_4$ polymorph. J Appl Phys 108(9):093519
69. Baran EJ (1976) Die Schwingungsspektren von $Ca_3(VO_4)_2$ und $Ca_3(AsO)$. Z Anorg Allg Chem 497:131–136
70. Parhi P, Manivannan V, Kohl S, McCurdy P (2008) Synthesis and characterization of $M_3V_2O_8$ (M = Ca, Sr and Ba) by a solid-state metathesis approach. Bull Mater Sci (India) 31(6):885–890
71. Ardanova LI, Chukova OV, Getman EI, Marchenko VI, Nedilko SG, Scherbatskyi VP (2002) Luminescent properties of the $Ca_5(VO_4)_3OH$ apatites with the heterovalence calcium replacement on alkali and rare-earth elements. Funct Mater 9(2):326–331

72. Sobszyk M, Szymański D (2013) A study of optical properties of Sm^{3+} ions in α-$Na_3Y(VO_4)_2$ single crystals. J Lumin 142:96–102
73. Song D, Guo C, Li T (2015) Luminescence of the self-activated vanadate phosphors $Na_2LnMg_2V_3O_{12}$ (Ln = Y, Gd). Ceram Int 41:6518–6524
74. Tamilmani V, Sreeram KJ, Nair BU (2015) Catechin assisted phase and shape selection for luminescent $LaVO_4$ zircon. RSC Adv 5(100):82513–82523
75. Boyko R, Chukova OV, Gomenyuk OV, Nagornyi PG, Nedilko SG (2005) Origin of red luminescence of sodium titanium phosphate crystals contained chromium and titanium ions. Phys Status Solidi 2(1):712–715
76. Chukova O, Nedilko S, Scherbatskyi V (2010) Luminescent spectroscopy and structure of centers of the impurity Eu^{3+} ions in lead tungstate crystals. J Lumin 130(10):1805–1812
77. Wybourne BG (1965) Spectroscopic properties of ions in crystals. Wiley, New York, p 236